Simulation and optimization of takeoff maneuvers of very flexible aircraft

Alfonso del Carre * and Rafael Palacios†
Imperial College, London SW7 2AZ, UK

A generic framework for the simulation of transient dynamics in nonlinear aeroelasticity is presented that is suitable for flexible aircraft maneuver optimization. Aircraft are modelled using a flexible multibody dynamics approach built on geometrically-nonlinear composite beam elements, and the unsteady aerodynamics on their lifting surfaces is modelled using vortex lattices with free or prescribed wakes. The open loop response to commanded inputs and external constraints is then fed into a Bayesian optimization framework, which adaptively samples the configuration space to identify optimal maneuvers. As a representative example, we demonstrate the proposed approach on a catapult-assisted takeoff. The specific modelling challenges associated to that problem are first discussed, including the effect of aircraft flexibility. An optimality measure based on ground clearance and wing root loads is then defined. It is finally shown that the link that ramp-length constraints introduce between acceleration, release speed and wing root loads is the main driver in the optimal solution.

I. Introduction

Advances in energy storage and generation and carbon fibre manufacturing have enabled High Altitude Long-Endurance (HALE) unmanned air vehicles whose stiffness is orders of magnitude lower than on conventional aircraft of similar dimensions. They display strong couplings between their (in general, nonlinear) aeroelastic and flight dynamics characteristics, which has brought about the development of suitable nonlinear aeroelastic simulation tools [1–5] and the appearance (or re-emergence) of less conventional dynamic stability situations [6, 7]. Geometrically-nonlinear effects in aeroelasticity are by now well known [8–10], specially in static analysis, and the dynamics of Very Flexible Aircraft (VFA) have already been investigated under multiple loading environments, including "1–cos" deterministic gusts [11], wake vortex encounters [12] and spanwise-varying low-altitude atmospheric turbulence [13].

A typical solar-powered HALE configuration has a large fraction of the total mass distributed along the wing span in the form of battery packs. This results in load distributions under longitudinal gusts that greatly vary with respect to conventional aircraft, where a large portion of the mass is in the fuselage or close to the wing root. Moreover, the

*Research Assistant, Department of Aeronautics, Room CAGB 308, South Kensington Campus.
†Professor of Computational Aeroelasticity, Department of Aeronautics, Room CAGB 338, South Kensington Campus, email: r.palacios@imperial.ac.uk, AIAA Associate Fellow

centre of mass variation in position when wings undergo nonlinear deformations can be important, due to a large ratio of the mass being attached to the wings. Finally, spanloaded lightweight airframes enhance the role of inertia relief as a passive load alleviation mechanism. To date, most of the computational effort in the open literature has focused on building nonlinear aeroelastic simulation strategies to capture those effects and, more recently, on designing suitable feedback control strategies [14–19]. An additional challenge is brought about by the need to identify nominal operation procedures, as recently explored by Maraniello and Palacios [20] for lateral maneuvers with very flexible wings. A parameterization of the maneuver definition defines an optimization problem on a suitable metric of the dynamic response of the vehicle. If the number of independent parameters used to define the maneuver is sufficient small, gradient-less methods become competitive in the exploration of the complex design space of feasible maneuvers. Many gradient-less algorithms, such as Powell [21] and Nelder-Mead [22] are still rather local and are designed to work sequentially, that is, one single cost function can be evaluated at a time. A more suitable family of algorithms is Bayesian Optimization (BO) [23, 24]. BO is now extensively used in machine learning for optimization of the hyperparameters of a learning model. It is suited for expensive cost functions defined in continuous domains with a relatively small dimensionality (typically less than 20). BO is based on the construction of a surrogate for the cost function and the estimation of the uncertainty of that surrogate using Gaussian process regression. This information is then used to determine where to sample next using a balanced trade-off between exploration versus exploitation.

As a working example, this paper will describe the modelling and implementation details, and the parameter choices for simulating and optimising the Catapult-Assisted Takeoff (CATO) of a representative solar-powered HALE aircraft. Robust and scalable launching procedures are of special interest as these vehicles evolve from experimental to commercial products. Depending on the total mass and geometry, the launch procedures found in the different prototypes under development include manual launch, a conventional runway takeoff or towing on a trailer. In particular, CATO offers reliability, predictability and robustness, while the relatively small footprint of the catapult would allow to easily modify the takeoff orientation. Importantly, takeoffs are good examples of aeroelastic simulation where no linearization can be carried out. The instantaneous aircraft velocity evolves from rest to close to cruise speed, while the structural deformation varies from a multiply-supported gravity-only loading condition to an aeroelastically trimmed shape. This happens in a few seconds. Finally, low wing bending frequencies imply that, for short enough ramps, the state of the aircraft on release might be highly dynamic and far from a steady climb condition.

This paper is divided in five sections, including this introduction. Section II describes the numerical methods used in this work. The nonlinear aeroelastic solver is first described, followed by a brief introduction to the optimization methods. Section III provides a description of the catapult-assisted takeoff problem. The aircraft model is first described, followed by implementation details and optimal maneuver definition. Numerical results can be found in section IV, which includes an assessment of elastic effects, an exploratory parametric study and the results from the optimization process. Lastly, section V summarizes the main outcomes of this work.

II. Numerical methods

For the aircraft simulations in this work a time-domain, geometrically-nonlinear aeroelastic solver has been built, which has been embedded in a general purpose Bayesian optimization framework. Both are summarized next.

A. Nonlinear aeroelastic simulation

1. Structural solver – Geometrically-Exact Composite Beams

The structural model presented here is a finite element beam formulation based on nodal displacements and rotations that uses quadratic elements for interpolation and Cartesian rotation vectors for the parameterization of finite rotations [25]. This formulation is particularly suitable for VFA aeroelasticity due to the support for geometrical nonlinearities and the ease of coupling with aerodynamic models and of implementation of boundary conditions and multibody constraints. A short description is included next, while further details can be found in Ref. [5].

Figure 1 shows the frames of reference involved in the description of the structural problem, and their relationship and parameterizations. The description of the deformation of the structure is given in a body-fixed, moving frame of reference A. Its kinematics with respect to the inertial frame, G, are defined by the instantaneous translational velocity $\boldsymbol{v}_A(t)$ and angular velocity $\boldsymbol{\omega}_A(t)$ of its origin. Subindexes are used to express that vector magnitudes are projected onto their components on a particular reference frame. We define the aggregated vector of rigid-body velocities $\boldsymbol{\beta} = \left\{\boldsymbol{v}_A^\top \boldsymbol{\omega}_A^\top\right\}^\top$.

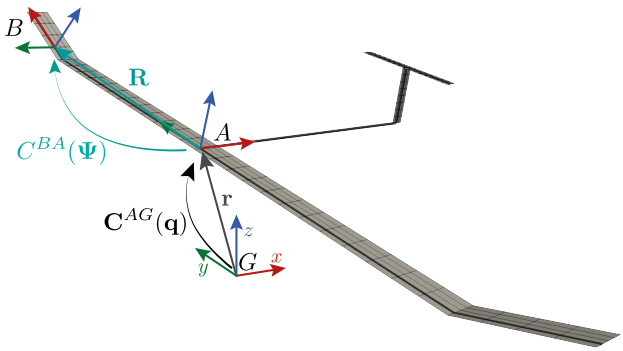

Fig. 1 T-Tail HALE configuration with frames of reference indicated.

The orientation of the body-attached frame of reference, A, with respect to the inertial frame, G, is parameterized using quaternions $\boldsymbol{q}(t) = \left\{q_0(t)\ \boldsymbol{q}_v(t)^\top\right\}^\top$, which gives a computationally efficient description of complex kinematics while avoiding accumulated errors and gimbal locking. They are obtained using the attitude propagation equations, $\dot{q}_0 = -\frac{1}{2}\boldsymbol{\omega}_A^\top \boldsymbol{q}_v$ and $\dot{\boldsymbol{q}}_v = -\frac{1}{2}\boldsymbol{\omega}_A q_0 - \frac{1}{2}\tilde{\boldsymbol{\omega}}_A \boldsymbol{q}_v$.

A coordinate transformation matrix is defined between each pair of reference frames. For the reference frame it can be written as $\boldsymbol{C}^{AG}(\boldsymbol{q})$, while for the i-th node of the finite-element discretization, it will be $\boldsymbol{C}^{BA}(\boldsymbol{\Psi}(s_i, t))$, with $\boldsymbol{\Psi}$ the local Cartesian rotation vector between the material frame B at position s_i and the aircraft frame A (see figure 1).

Defining the elastic state vector $\boldsymbol{\eta}$ by concatenating all nodal displacements and rotations, with respect to the body-attached reference frame A, the discretized equations of motion can be written as [5]

$$\boldsymbol{\mathcal{M}}(\boldsymbol{\eta}) \begin{Bmatrix} \ddot{\boldsymbol{\eta}} \\ \dot{\boldsymbol{\beta}} \end{Bmatrix} + \begin{Bmatrix} \boldsymbol{\mathcal{F}}^{S}_{\text{gyr}}(\boldsymbol{\eta}, \dot{\boldsymbol{\eta}}, \boldsymbol{\beta}) \\ \boldsymbol{\mathcal{F}}^{R}_{\text{gyr}}(\boldsymbol{\eta}, \dot{\boldsymbol{\eta}}, \boldsymbol{\beta}) \end{Bmatrix} + \begin{Bmatrix} \boldsymbol{\mathcal{F}}_{\text{stiff}}(\boldsymbol{\eta}) \\ 0 \end{Bmatrix} = \boldsymbol{\mathcal{F}}_{\text{ext}}(\boldsymbol{q}, \boldsymbol{\eta}, \dot{\boldsymbol{\eta}}, \ddot{\boldsymbol{\eta}}, \boldsymbol{\beta}, \dot{\boldsymbol{\beta}}), \tag{1}$$

where $\boldsymbol{\mathcal{M}}(\boldsymbol{\eta})$ is the discrete mass matrix, which in general includes couplings between the elastic and the rigid-body degrees of freedom. The discrete gyroscopic and stiffness forces are represented by $\boldsymbol{\mathcal{F}}_{\text{gyr}}$ and $\boldsymbol{\mathcal{F}}_{\text{stiff}}$, respectively, while the discrete external forces, $\boldsymbol{\mathcal{F}}_{\text{ext}}$, include gravitational, propulsion (modelled as point forces), and aerodynamic forces. The latter ones are described below. The instantaneous position of the body-attached frame A with respect to the inertial frame of reference is finally integrated in a postprocessing step.

Additional constraints may be needed on the flexible aircraft equations when modelling multibody problems (e.g., hinged winglets) or for problems with forced displacements (as in the catapult-assisted takeoff). This is done here with an augmented Lagrangian formulation [26], which results in a better control of the conditioning number of the constrained equations and a regularization of the Hessian to increase numerical robustness. Finally, the resulting system is integrated in time using a conventional Newmark-β scheme with artificial dissipation [25].

2. Aerodynamic solver – The Unsteady Vortex-Lattice Method

As we consider problems driven by lifting forces, potential flow theory has been used. Lifting surfaces are modelled by a structured lattice of rectilinear vortex ring elements. Every surface has a wake associated with it, idealized as a thin vortex sheet that extends a certain distance downstream, or until infinity for static simulations with horseshoe vortex wake modelling. Circulation is then computed at every vortex ring such that the normal velocity at the collocation points is zero. Here, the collocation points are placed at the centre of vortex rings, which are further displaced one fourth of their streamwise length downstream along the wing chord. This has been shown to improve the convergence of the pitching moment [27]. Defining $\boldsymbol{\Gamma}$ and $\boldsymbol{\Gamma}_w$ as the vectors of the circulation on all bounded and wake panels, respectively, the non-penetrating boundary conditions can be written as

$$(\boldsymbol{\mathcal{A}}\boldsymbol{\Gamma} + \boldsymbol{\mathcal{A}}_w\boldsymbol{\Gamma}_w + \boldsymbol{v}) = 0, \tag{2}$$

where $\boldsymbol{v}$ is the vector with the instantaneous normal velocity (*normalwash*) at all the collocation points, which includes structural velocities, rigid body motion contributions and background flow in a non-stationary atmosphere. Matrices $\boldsymbol{\mathcal{A}}$ and $\boldsymbol{\mathcal{A}}_w$ are the aerodynamic influence coefficient matrices, which are recomputed at each time step using Biot-Savart law on the current geometry. Wake circulation is convected downstream at each time step and the Kutta condition is

enforced by convecting the circulation at the trailing edge onto the adjacent wake panel at each time step. Finally, the forces on the wet surfaces are calculated using the unsteady vector form of the Joukowski theorem [28], which includes circulatory and non-circulatory effects and resolves all force components (in particular, induced drag) for arbitrary kinematics.

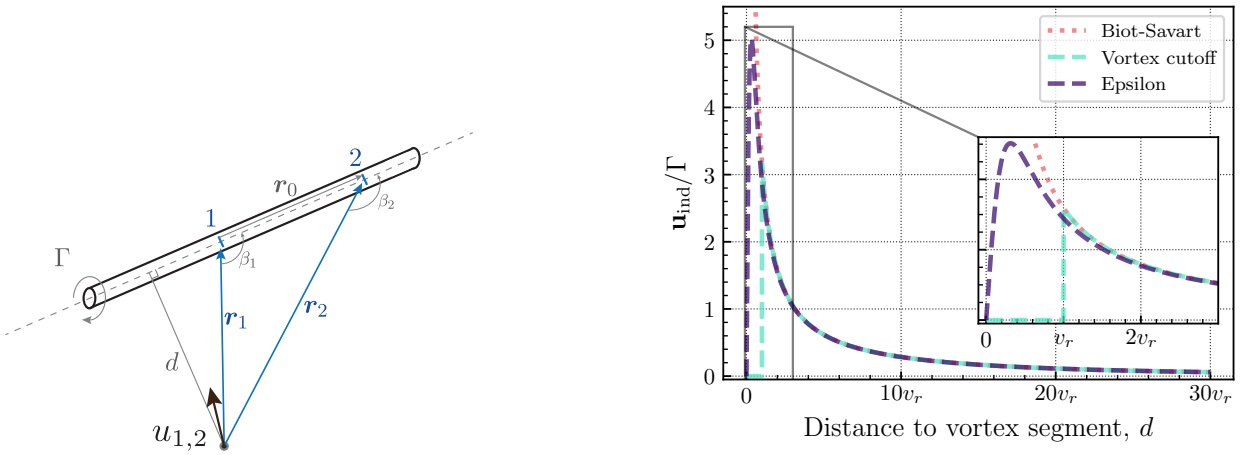

(a) Definitions in the Biot-Savart law on a vortex segment.

(b) Induced velocity for a vortex segment with different vortex models.

Fig. 2 Geometry definition and effect of desingularization approach in the Biot-Savart law

The Biot-Savart law used in the UVLM requires a desingularization strategy when the distance d between the collocation point and the vortex segment goes to zero (see figure 2a). Typically a vortex core radius is introduced [27], whose value is dependent on the problem geometry and dynamics. For our problems of interest, a vortex core value that is large enough to avoid numerical problems when $d \to 0$ was found to influence the solution. The approach to solve this has been to reformulate the Biot-Savart law while introducing a desingularization coefficient ϵ_v as

$$\boldsymbol{u}_{1,2} = \frac{\Gamma}{4\pi} \frac{\boldsymbol{r}_1 \times \boldsymbol{r}_2}{|\boldsymbol{r}_1 \times \boldsymbol{r}_2|^2 + \epsilon_v} \boldsymbol{r}_0 \left(\frac{\boldsymbol{r}_1}{r_1 + \epsilon_v} - \frac{\boldsymbol{r}_2}{r_2 + \epsilon_v} \right), \tag{3}$$

which ensures ensures that $\lim_{d \to 0} \|\boldsymbol{u}\| = 0$. The suitable value for it has been observed to be case independent if (3) is written in dimensionless form. In our implementation, where distances are normalized by the wing root chord, its value is fixed at $\epsilon_v = 10^{-8}$. Figure 2b shows the induced velocity variation with distance to the vortex segment for the unmodified Biot-Savart law, as well as those obtained with a vortex-core cutoff the current desingularization strategy, equation (3), which is referred to as *Epsilon* in the figure.

3. Aeroelastic coupling

The structural and aerodynamic solvers described above have been strongly coupled using a Block Gauss-Seidel algorithm. Both solvers are therefore run once per FSI iteration. The mapping of forces and moments from the

aerodynamic grid to the structural nodes (and of displacements in the inverse mapping) does not require any interpolation, as the beam nodes define the spanwise discretization of the aerodynamic grid. The lifting surfaces cross section is assumed to be rigid and aerodynamic forces in each vertex result in a force and moment pair at the associated structural node. Having matching grids brings a small computational penalty but substantially simplifies the generation of 3D displacement fields derived from the beam model. The spatial resolution is determined through convergence of aeroelastic results, although, in practice, a converged spanwise discretization of the aerodynamic grid is also often suitable for the structural solver.

The convergence criterion for the subiterations in the time-marching aeroelastic simulations is based on two residuals, one that depends on the structural displacements of all beam nodes, $\boldsymbol{\eta}$, and a second on its time derivative, $\dot{\boldsymbol{\eta}}$. For each of them, the relative 2-norm between two subiterations is computed and normalized with the amplitude of the current solution. Iteration is carried out to convergence, including an adaptive Aitken relaxation factor $\omega \in [0, 1)$ that acts on the applied forces on the structure $\mathcal{F}^n_{ext,k}$ (for the k-th iteration of the n-th time step) such that

$$\mathcal{F}^n_{ext,k}\Big|_{\text{relaxed}} = (1-\omega)\,\mathcal{F}^n_{ext,k}\Big|_{\text{original}} + \omega\,\mathcal{F}^n_{ext,k-1}\Big|_{\text{original}}. \tag{4}$$

A linear evolution of the relaxation factor has been chosen within each time step of the FSI loop. A typical initial value is $\omega \simeq 0.3$, while edge of the envelope conditions (specially close to overspeed cases) might require $\omega > 0.6$.

Running a strongly-coupled simulation with the previously mentioned wake shedding procedure imposes a hard constraint in the choice of time step. While the lifting surface chordwise discretization has some effect on it, the overall cost of the simulation is ultimately driven by the number of vortex rings in the wake. A common workaround in weakly coupled simulations is to run multiple time steps of the structural solver while maintaining the aerodynamic loads constant. This effectively decouples both solvers time steps, provided that the relevant dynamics are slow enough compared to the time step. However, in complex maneuvers, such as those considered here, assuming constant aerodynamic forces between aerodynamic time steps often makes solutions to diverge. A custom formulation that allows to run a strongly coupled simulation while providing a certain degree of decoupling has therefore been developed and is outlined in figure 3: Structural sub-steps are run in the FSI iteration scheme, while aerodynamic loads, applied forces and time-dependent constraints on the structural solver are linearly interpolated during FSI iterations between the previous time step (Q_{s-1}) and the last FSI iteration of the current aerodynamic time step (Q^k_s). Forces are introduced as follower forces and their orientation is updated every structural sub-step. Flight dynamics variables are integrated every structural time step.

An additional challenge in the aeroelastic simulation of vehicles with very low wing loading is associated to the added mass in the unsteady aerodynamics. At low altitudes, added mass is comparable to the local inertia of the wing sections and this can destabilize the convergence in the FSI loop. This is avoided here by ramping the added mass

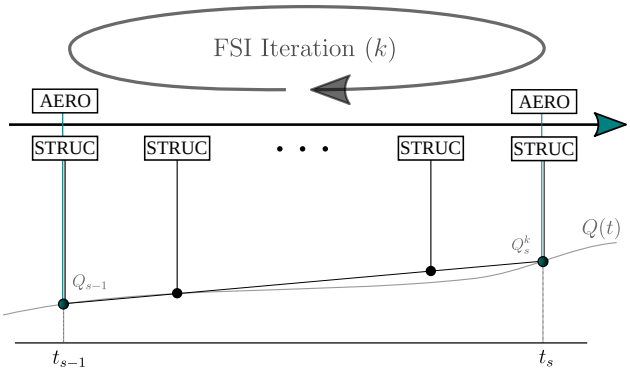

Fig. 3 Subiteration process in the strongly coupled FSI scheme.

during the first FSI subiterations, such that the first iteration is computed without added mass terms. Finally, to mitigate for the slow relatively convergence in the time derivative of the circulation, which feeds through into the added mass forces, a Wiener filter [29] has been included. In our implementation, the noise is estimated from all available time history of the circulation rates and the only required input is the smoothing value, given as a window length.

4. Implementation

All simulations have been run in `SHARPy` (Simulation of High Aspect-Ratio aeroplanes in Python). `SHARPy` focuses on efficiency, robustness and ease of use for developers and users. The main code of `SHARPy` is written in Python 3, while some computationally expensive routines, such as the structural and aerodynamic solvers, are coded in modern Fortran or C++. The code has been developed as a collaborative platform, and thus, it has been built in a modular way, allowing for seamless expansion through user contributions. Hosted in GitHub, `SHARPy` is built in an environment with version control, automatic documentation generation, continuous integration and code coverage monitoring. The software is available under a BSD 3-Clause Open-Source License [30], and the distribution online includes multiple fully-documented test cases used for verification of the implementation against the literature. Detailed code-to-code verification on the X-HALE platform [31] has also been presented in Ref [32].

B. A Bayesian optimization framework for complex maneuver definition

Let $\boldsymbol{x} \in \mathcal{X} \in \mathbb{R}^n$ be a parameterization of the space of possible maneuvers under consideration. Here, $\mathcal{X}$ is the specified domain and n is the dimensionality of $\boldsymbol{x}$. An optimization problem is then defined with a cost function $\boldsymbol{J}(\boldsymbol{x}) \in \mathbb{R}$. Adding a set of unilateral constraints $\boldsymbol{\Phi}(\boldsymbol{x})$, the problem can be written as

$$\min_{\substack{\boldsymbol{x}\in\mathcal{X};\\ \boldsymbol{\Phi}(\boldsymbol{x})\leq 0}} J(\boldsymbol{x}). \tag{5}$$

1. Surrogate construction

A BO framework requires two components: first, a *Bayesian statistical model* of the objective function, and, second, an *acquisition function* that decides where the cost function will be sampled next [23]. Typically, the model is first initialized with a set of evaluations designed to cover the parametric space, such as a latin hypercube sampling. However, since complex constraints are sought here, that structured initialization is not feasible and the points are taken instead at random from inside the valid domain. After that initial sampling, the remainder of a budget of N_{eval} function evaluations is allocated iteratively following Algorithm 1.

while $n \leq N_{eval}$ **do**
  Update the posterior probability distribution on J using all the available data;
  Let x_n be a maximiser of the acquisition function over x, where the acquisition function is computed using the current posterior distribution;
  Observe $y_n = J(x_n)$;
  Increment n;
end
Return a solution: either the point evaluated with the largest $J(x)$, or the point with the smallest posterior mean;

Algorithm 1: Simple pseudo-code for BO, adapted from [24].

The statistical model of the objective function is defined as a Gaussian process regression. It provides a posterior probability distribution of potential values of $J(\boldsymbol{x})$ at a candidate $\boldsymbol{x}$. A posterior probability distribution is the assigned conditional probability after the cost function has been evaluated. Every observation of J is introduced in the Gaussian process, and the posterior probability distribution is updated. Finally, with the posterior distribution as input, the acquisition function estimates the value of the function at a new point $\boldsymbol{x}$. We use as acquisition function the Expected Improvement, which offers a trade-off between expected mean value and model uncertainty. Once the BO has approached the solution and the function has been evaluated around the global minimum, the uncertainty of the Gaussian-process surrogate in that region is very low and therefore other points of the parametric space are sampled instead. This, which is one of the strengths of BO, turns out to also slow down convergence in the final stages of the optimization process. An alternative strategy for local refinement is therefore used and it is described next.

2. Local refinement of the solution

Once the *global* optimization described above has found a potential minimum, a *local* method is used to refine the solution [33, 34]. Typical basin-hopping approaches require either a rather large number of additional function calls or gradient/Hessian information. As evaluations to our cost function are expensive, we use instead the information contained in the Gaussian process regression of the BO to construct a surrogate of the cost function. Moreover, the BO framework is used as an adaptive sampling algorithm to increase the accuracy of the surrogate near the optimum.

After building this surrogate from the trained Gaussian process, we need to add the constraints so that the local optimizer does not converge towards a point outside the domain. Local optimizers that allow to impose constraints are

usually more expensive or present slower convergence rates. Instead, the bounds have been enforced here as a penalty. The local optimizer used in this work is the Powell [21] implementation in SciPy. While gradient-based algorithms are available, and usually outperform non-gradient based ones, enforcing constraints through a penalty approach generates an artificially abrupt step in the value of the function in our problem. This then results in convergence problems as the Jacobian is estimated through finite difference methods.

3. Implementation

The implementation of the optimizer used is the one distributed in `GPyOpt` [35]. This framework supports simple bounds constraints in the parameters, as well as unilateral constraints expressed as inequalities based on the input parameters. The call to `SHARPy` is done in a manner that avoids the race conditions that could potentially arise from the parallel execution of the cost function evaluation. The input/output for every case is handled independently, from separate folders, by parallel subprocesses running an instance of `SHARPy` each.

III. Vehicle and maneuver definition

To exemplify the previous approach we consider the optimization of a catapult-assisted takeoff on a representative VFA model. This section covers the vehicle definition, the description and parameterization of the maneuver, and the cost function definition.

A. The T-Tail HALE model

The vehicle used in this study is a simple single fuselage T-tailed very flexible aircraft. The geometry (figure 4) and stiffness and mass data (table 1) have been previously used in Refs. [12, 13]. This aircraft features a large aspect ratio and low structural weight, with the payload (50 kg) located at the fuselage-spar intersection. Longitudinal control is provided by the all-moving horizontal stabilizer that deflects around the elastic axis location, while lateral control is granted though a rudder in the vertical stabilizer with a chord of 50% of the fin chord. All the lifting surfaces in this aircraft are assumed to be symmetric and they are modelled as flat plates in the UVLM. The elastic axis of the main wing is located at 30% of the chord and it is coincident with the centre of mass of the cross-section. The tail control surfaces have their elastic axis and cross-sectional centre of gravity located at 50%.

Stiffness at the elastic axis is shown in Table 1. These are given in material frame of reference (noted as B in figure 1). Isotropic properties are used with EA the axial stiffness, GJ the torsional stiffness, EI_y the out-of-plane bending stiffness, and EI_z the in-plane stiffness. The shear stiffness constants, GA_y and GA_z, have been chosen high enough to dismiss the effect of these degrees of freedom (in this case, $1 \times 10^5\,\mathrm{N\,m^2}$). The cross-sectional moments of inertia in the mass matrix $\mathrm{diag}\left(I_{xx}, I_{yy}, I_{zz}\right) = \left(\bar{J}, \bar{J}/2, \bar{J}/2\right)$ have been chosen such that $I_{xx} = I_{yy} + I_{zz}$. This configuration presents large wing deformations even in steady horizontal flight ($\sim 24\%$). Due to the effective dihedral, there are strong

Component	EA [N m^{-1}]	GJ [N m^2]	EI_y [N m^2]	EI_z [N m^2]	$\bar{m}$ [kg m^{-1}]	$\bar{J}$ [kg m]
			Flexible			
Wing	1.5×10^7	1.5×10^4	3.0×10^4	6.0×10^5	0.75	0.075
Fuselage	1.5×10^8	1.5×10^5	3.0×10^5	6.0×10^6	0.2	0.08
Fin	1.5×10^8	1.5×10^5	3.0×10^5	6.0×10^6	0.3	0.08
Tail	1.5×10^8	1.5×10^5	3.0×10^5	6.0×10^6	0.3	0.08
			Very Stiff			
Wing	1.0×10^8	5.0×10^5	1×10^6	2.0×10^7	0.75	0.075
Fuselage	1.0×10^9	5.0×10^6	1×10^7	2.0×10^8	0.2	0.08
Fin	1.0×10^9	5.0×10^6	1×10^7	2.0×10^8	0.3	0.08
Tail	1.0×10^9	5.0×10^6	1×10^7	2.0×10^8	0.3	0.08

Table 1 Structural properties of the T-tail HALE model.

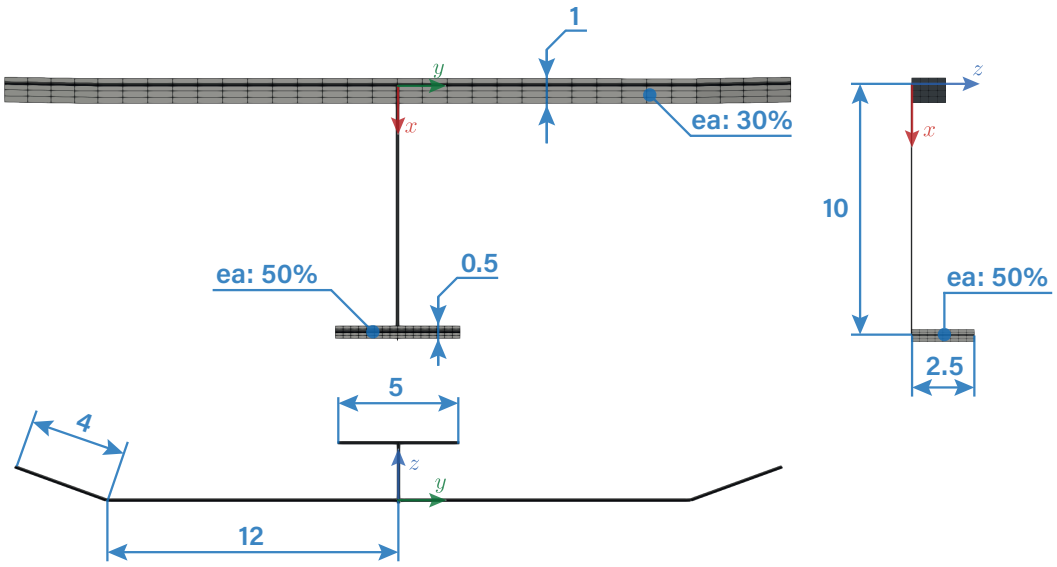

Fig. 4 Description of the T-tail HALE model. All units in metres. Figure also includes the UVLM discretization.

couplings between in-plane bending and torsion.

variations of less than 2.5% in angle of attack, elevator deflection and thrust with respect to a model with 16 chordwise panels in all surfaces and twice as many spanwise elements. The aircraft is trimmed for level flight at 10 m s^{-1} and the trim parameters for this condition are given in table 2. All simulations are run using a prescribed wake for the UVLM, that is, the wake is convected with the background flow and not by self-generated induced velocity. Finally, an investigation onto ground effects showed that they are negligible for such light vehicle and they have not been included in the simulations.

The mixed coupling formulation introduced in section II.A.3 increases the order of the approximation of the aerodynamic loads and provides more accurate results for a given time step when compared to a weakly coupled simulation. While the number of evaluations of the structural solver is increased, a coarser aerodynamic spatial

Variable	Flexible	Very Stiff
Angle of attack, α [°]	4.072	3.81
Control surface deflection, δ [°]	-1.27	-0.76
Rudder deflection, δ_r [°]	0.00	0.00
Thrust, T [N]	3.87	3.76
Total mass [kg]	78.25	
Wing surface [m^2]	32.00	
Wing loading [$kg\,m^{-2}$]	2.44	

Table 2 Trim values for the flexible and very stiff T-tail HALE model at $10\,m\,s^{-1}$.

discretization and the increased accuracy of the strongly coupled simulations—specially when including rigid body motions— result in substantial computational saving for highly dynamic cases. In particular, the model used in this work has second in-plane bending mode frequency of around 14 Hz in its cruise shape. Based on the chordwise discretization and the cruise speed, the FSI—and aerodynamic—time step for the simulation has been chosen $\Delta t = 2.5 \times 10^{-2}$ s, which equates to a Nyquist frequency of 20 Hz. While the second in-plane bending mode would be captured if the structural solver was run with the same time step than the FSI, the accuracy of the beam dynamics would be compromised. With the in-plane bending component of the dynamics being of such importance for this particular problem, this simulation has been run with $\Delta t_{\text{struct}} = 0.5\Delta t_{\text{FSI}}$. This doubles the Nyquist frequency for the structural solver, which has been deemed high enough to capture the relevant dynamics of the problem.

B. Catapult-assisted takeoff

Vehicles in this category are rarely designed to sustain its own weight in the ground. Consequently, the aircraft is fist attached to the catapult in multiple points of the wings and fuselage (those attachment points are also assumed to be rigidly linked among themselves, as they would be on a moving part of the catapult), then accelerated along a prescribed trajectory (a *ramp*), and finally released when a certain speed is reached. Only displacement constraints are enforced at the attachment points. A straight ramp is assumed, defined by its angle with respect to the ground, Γ_R. The aircraft is mounted on the catapult with an additional offset angle θ_o, as shown in figure 5. Its attitude angle with respect to the horizontal is $\alpha_{\text{cruise}} + \theta_o$, with α_{cruise} the cruise angle of attack shown in table 2. A reference root angle of attack is defined while in the ramp by subtracting the ramp angle, Γ_R, to that attitude angle. A constant acceleration, a, is assumed through the takeoff. Lastly, the release speed of the aircraft is also a parametric value identified as v_r.

In addition to the previous four parameters and associated assumptions (straight takeoff trajectory, constant acceleration), some constraints need to be imposed. Firstly, a maximum ramp length is defined by means of a unilateral (inequality) constraint, as shown in figure 6. Secondly, the angle of attack of the aircraft during the launch is limited to be under the stall limit. As our model is based on potential flow theory, this is enforced by a constraint on the incidence angle, $\alpha_{\text{cruise}} + \theta_o - \Gamma_R$ (figure 6). The parametric domain that is studied in this paper is therefore a combination of

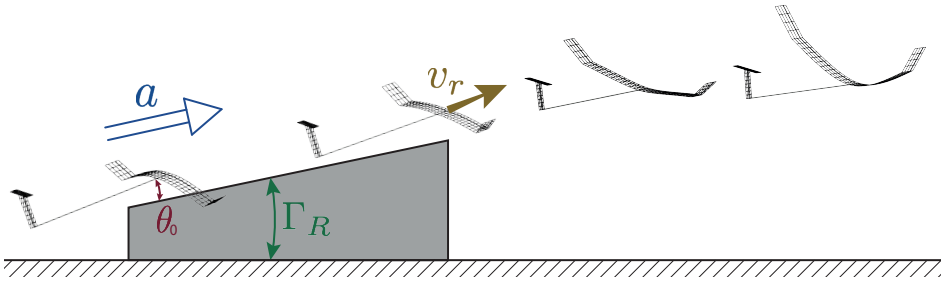

Fig. 5 Parameters in the catapult-assisted takeoff. The aircraft goes from rest on the left to level flight on the right

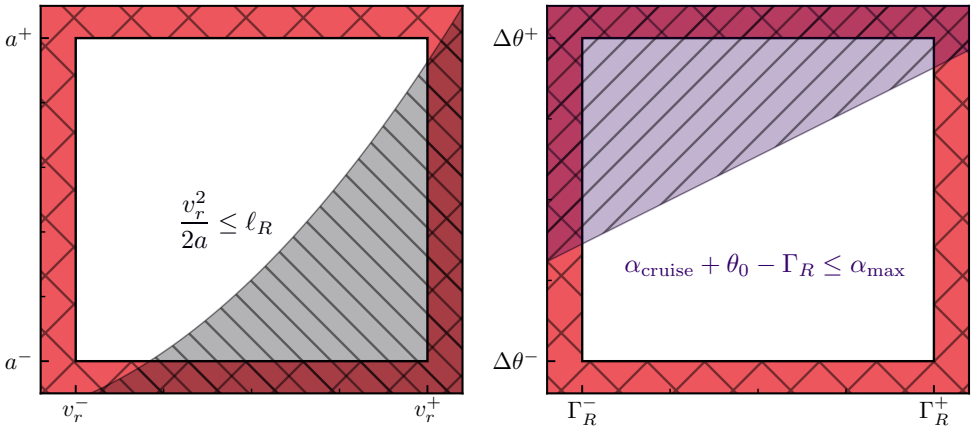

Fig. 6 Parameter space with bounds in red and ramp length and angle of attack constraints in green and purple, respectively.

bounds for the four parameters plus the added constraints of the ramp length and incidence angle.

During takeoff, the aircraft is subject to the reaction forces at the clamping points. These reaction forces depend on the dynamics of the aircraft structure and the aerodynamic forces that change with the structural deformation and the imposed acceleration. When the aircraft is at rest, the reaction forces only counteract the gravity. As the aircraft is accelerated, the inertial and stiffness effects also need to be counteracted in order to enforce a smooth trajectory and acceleration profile. In the final stages of the CATO, the aerodynamic effects are dominant and the clamping forces act to keep the aircraft from deviating from the path by taking off too early, avoiding structural deformations between clamping points, and potentially fighting the increase in drag due to the lift generation. To exemplify this, figure 7 shows the instantaneous shape of the aircraft on a baseline CATO (see table 3), together with the wing tip deflection (in percentage of the semispan) with respect to the jig shape.

The clamping point location is therefore an important factor in a catapult-assisted takeoff. As a rule of thumb, a catapult built with a shape which is close to that of the aircraft in the cruise state would results in smaller structural loads and variations in altitude. This would not be however a practical solution, and our approach has been to study the effects of large structural deflections throughout the whole maneuver. This requires a more challenging numerical setup

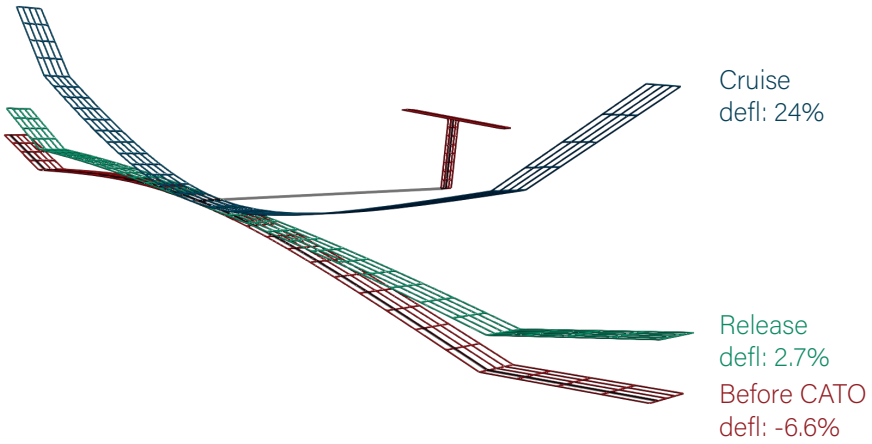

Fig. 7 Snapshots of the aerodynamic grid and wing tip deflections at different stages of the baseline CATO.

Acceleration, a	4.10 m s^{-2}
Release speed, v_r	10.77 m s^{-1}
Ramp angle, Γ_R	7.26°
Attitude offset, θ_o	4.87°

Table 3 Baseline for parametric study

but a much smaller catapult. The results shown here are simulated with the aircraft supported in three points: on both sides of the wing root, separated 1 m from the root, and the fuselage-fin intersection. The release occurs simultaneously in all three points.

C. Simulation process

Simulation of the CATO is split in the three stages shown in figure 8: *initial stage*, *launch stage* and *free flight*. During the initial and launch stages, the nodal velocity constraints are active, while the free-flight stage is a nonlinear aeroelastic simulation including rigid body dynamics. The initial stage defines the equilibrium shape of the aircraft on the catapult at rest under gravity loads. A background flow (incoming wind) velocity is assumed and 0.5 m s^{-1} has been set as a default. For convenience in our implementation, the initial equilibrium is found from a dynamic aeroelastic solution starting with undeformed airframe. During the solution, the aerodynamic wake is convected using the background flow velocity. As a result, the wake length during this stage (*initial* stage in figure 8) is sensibly shorter than in free flight. The robustness of the vortex-induced velocity model, as described in section II.A.2, is critical here because the distance between the wake vortex segments and the trailing edge can be small enough to cause numerical instability.

Once the structural state of the configuration has approached the steady-state gravity-only deformation, the launch stage is started. The three components of the velocity of the attachment points are prescribed based on the launch parameters as a function of time. This stage is the most demanding from a numerical robustness point of view. The

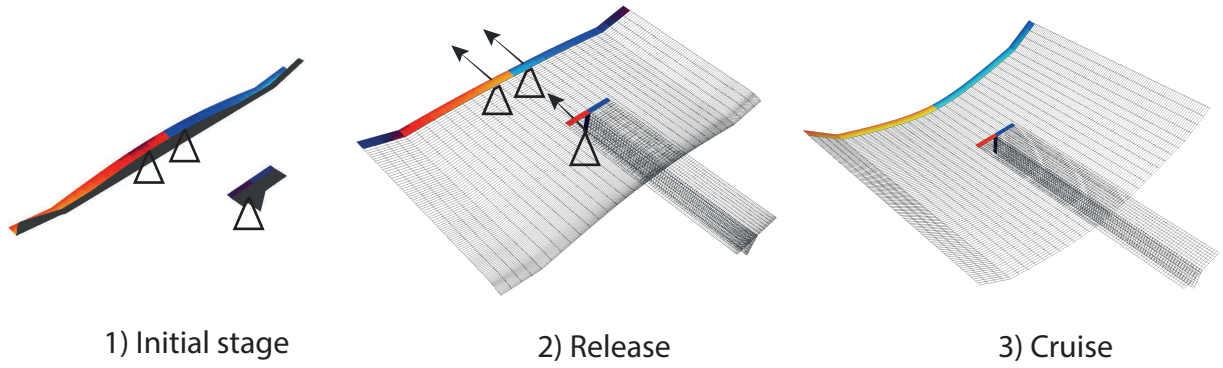

Fig. 8 Three steps of the CATO process, showing an increasing wake length as the aircraft velocity increases.

first part of the launch is dominated by inertia effects, where the mass distributed along the high aspect-ratio wing is suddenly accelerated from a clamping point located near the wing root. In addition, as the wing generates more lift, its geometry is modified, which can result in geometrical couplings that did not exist in the first stages of the launch, where the low dynamic pressure and relatively fast acceleration, together with the generally slow dynamics of the wing, can result in small deformations. As the CATO progresses, dynamic pressure increases, unsteady aerodynamics plays a more important role, and the wake extends several chords downstream. Unsteady aerodynamics result in damped wing out-of-plane bending dynamics, while in-plane and torsion dynamics are geometrically coupled due to the effective dihedral and are relatively undamped. The release from the ramp is a critical point from a numerical stability point of view. The structural solver goes from a constantly accelerated motion enforced through nodal constraints to an unsteady free-flight simulation.

After the release, the aircraft dynamics are simulated in open-loop, with the trim parameters set for cruise flight. This decision is due to two reasons: first, it reduces the complexity in the simulation and the analysis, and second, existing solar-powered HALE configurations generally do not feature high-authority flight control systems due to their very specific mission, payload and requirements. We note also that the typical climb rates are so small that optimizing launch for initial level flight or climb fundamentally gives the same outcome.

D. Optimal maneuver definition

Once the problem has been defined, it is necessary to provide a way of quantifying the suitability of the different maneuvers based on the values of the parameters. While multiple cost functions can be defined for this maneuver and several were investigated in preparation of this work, the selected cost function will minimize 1) ground clearance after takeoff and 2) structural root loads, for different (prescribed) available runway lengths.

The ground clearance is quantified as the minimum value of the body-attached frame of reference vertical coordinate with respect to the $z = 0$ plane evaluated after release. While low—or negative—values of ground clearance can

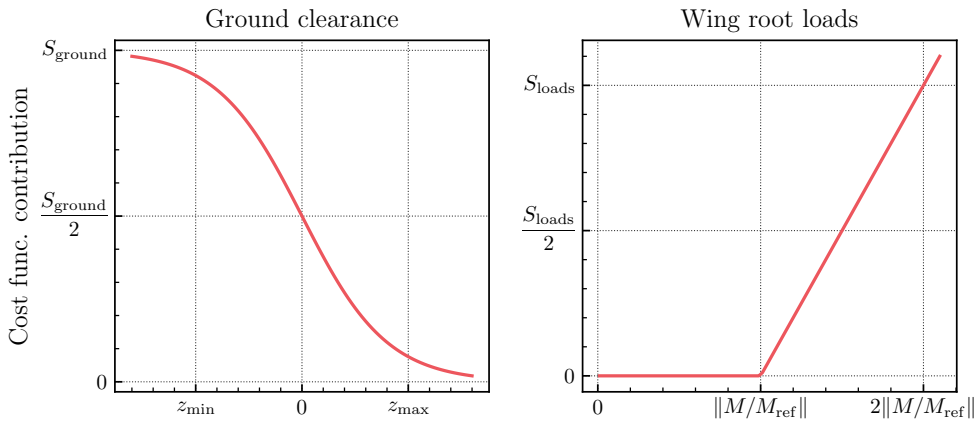

Fig. 9 Cost function contributions associated to the ground clearance (left) and wing root loads (right).

obviously be considered bad performance, relatively high values of ground clearance past a certain point do not improve the suitability of the maneuver anymore. Due to this, the function chosen to map the ground clearance to a penalty term in the cost of the takeoff is a sigmoid such as

$$J_{\text{ground}} = \frac{S_{\text{ground}}}{1 + \exp\left(\tilde{z} - \frac{1}{2}\right)}, \tag{6}$$

with $\tilde{z} = (z - z_{\min})/(z_{\max} - z_{\min})$, and $z_{\min}$ and $z_{\max}$ given constants with the minimum and maximum clearances described previously (see figure 9). Finally, S_{ground} is a scaling factor.

Three wing root loads are considered: torsion, out-of-plane bending and in-plane bending moment. Being $\mathbf{M}_{\text{ref}}$ the moments of the wing root in cruise at $10\,\text{m}\,\text{s}^{-1}$, and $\mathbf{M}$ the instantaneous root moments at a time t, the contribution of the wing root loading to the cost function is defined as

$$J_{\text{loads}} = \sum_{k=1}^{3} \max_{t} \left(\left| \frac{M^k}{M^k_{\text{ref}}} \right| - 1 \right) \cdot S^k_{\text{loads}} \tag{7}$$

where $\boldsymbol{S}_{\text{loads}} \in \mathbb{R}^3$ is a scaling vector. The overall shape of this contribution is shown in figure 9. The final cost function gives equal weight to both contributions, that is, $J = J_{\text{ground}} + J_{\text{loads}}$.

IV. Numerical Results

A. Flexibility effects on a catapult-assisted takeoff

Baseline CATO parameters have been established after a preliminary numerical exploration and they are given in table 3. It corresponds to a runway length $\ell_R = 14.15\,\text{m}$ and incidence angle $\alpha_{\text{cruise}} + \theta_0 - \Gamma_R = 1.68°$. For this maneuver, two configurations are considered: a *very flexible aircraft*, defined as in table 1, and a *stiff aircraft*, obtained

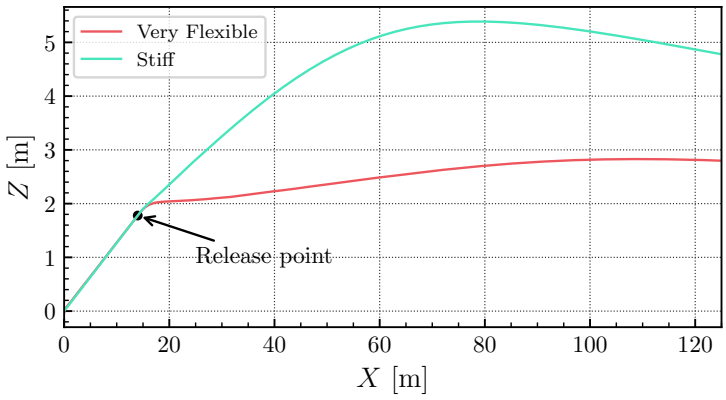

Fig. 10 Longitudinal trajectory during CATO of the T-tail HALE in its flexible and rigid variants. The parameters of the launch can be found in table 3.

by multiplying all stiffness constants by a factor of 33. Figure 10 shows the longitudinal trajectory of the wing root node as seen from an Earth system. From a ground clearance point of view, the very flexible aircraft presents good performance, as its lowest point after release is effectively the release point. However, the differences with the stiff aircraft are stark. With the given maneuver definition, the stiff aircraft is released near its steady-state condition, with just a small pitch angle deviation from the cruise conditions and a slightly greater speed than the original cruise speed. Shortly after release, the response of the stiff aircraft is dominated by its phugoid mode, which is slow enough that it could be further damped using a very basic flight controller.

Figure 11 presents the three components of the wing root moments, normalized by the $10\,\mathrm{m\,s^{-1}}$ cruise root loads of the very flexible aircraft (for the flexible and stiff aircraft results). The first 1.5 s in the simulation correspond to the initial stage in figure 8, where the aircraft finds its equilibrium on a stationary catapult. The out-of-plane (OOP) bending moment therefore drops for both configurations. During the launch stage this moment can be seen to increase much faster on the stiff aircraft than on the very flexible one. This is mainly due to the fact that the rigid configuration gravity-only shape is very similar to the jig and cruise shapes. It is also important to note the large damping of the out-of-plane oscillations, together with its very limited coupling with the other degrees of freedom. The torsion and in-plane (IP) dynamics oscillate at the same frequency with no phase delay due to geometrical coupling. In addition, the oscillatory behavior of these two degrees of freedom is only lightly damped. This is due to the much smaller aerodynamic damping in these motions when compared to the out-of-plane bending. It is important to note that, unlike other common aerodynamic solvers such as DLM, the aerodynamic solver used in these results accounts for the incident velocity contribution of the in-plane motion of the structure. This includes lift as well as induced drag variations. The details on the process followed for obtaining the aerodynamic forces from the UVLM solutions in a more general way than the usual method described in Ref. [27] can be found in Ref. [28]. Moreover, although the steady flight deformations of the models are substantially different, the wing root bending loads are not dissimilar, as they are driven

by the total weight distribution, which is the same in both models. The differences in torsion loading are more marked due to the large effective dihedral of the very flexible aircraft, which results in a different compensation of the induced drag component of the aerodynamic forces. In fact, the wing tip structural element of the stiff configuration has a dihedral angle of 20°, the jig shape one, while the very flexible configuration presents an effective dihedral angle of 38°.

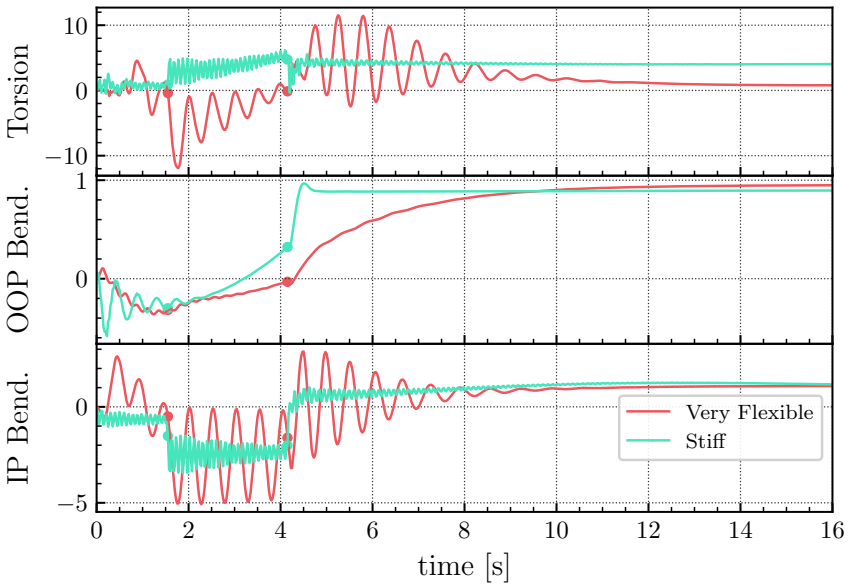

Fig. 11 Torsion, out-of-plane and in-plane wing root loads during CATO for the very flexible and the stiff T-tail models. The parameters of the launch can be found in table 3. Dots indicate start/end of launch stage and values are normalized with cruise wing root loads.

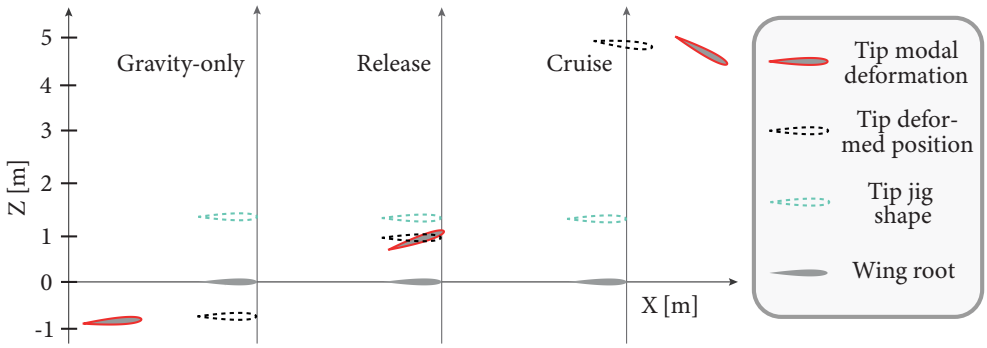

Fig. 12 Position of the wing tip cross section of the flexible model at different stages of the CATO. Position for the jig shape, aeroelastic shape and second vibration mode with the former as reference condition.

Lastly, in order to better understand the variation of the characteristics of the structure during the different stages of the takeoff, the first natural vibration modes (without aerodynamics) of the very flexible aircraft have been calculated from the tangent mass and stiffness corresponding to three different conditions, namely, the aircraft at rest (gravity only), at the release point, and in cruise. The results at the release point have been calculated with the non-equilibrium conditions

Mode	Gravity-only		Release		Cruise	
	Freq [Hz]	**Type**	**Freq** [Hz]	**Type**	**Freq** [Hz]	**Type**
1st mode	0.449	OOP (I)	0.438	OOP (I)	0.419	OOP (I)
2nd mode	1.83	IP/torsion	1.81	Torsion/IP	1.34	IP/Torsion
3rd mode	2.72	OOP (II)	2.71	OOP(II)	2.61	OOP (II)

Table 4 First three natural vibration frequencies of the very flexible model at different stages of the CATO.

as reference. Table 4 shows the frequencies of the first three vibration modes, together with their characterization. While out-of-plane bending modes do not fundamentally change with the configuration, the second mode in the table, which is a coupled in-plane/torsion mode, shows large changes. This is further investigated in Figure 12, which shows the projection on the plane of symmetry of the aircraft of the wing tip section for this second vibration mode. A normalized mode shape is superimposed on the tip deformed position, which is also included in the figure. As it can be seen, the second natural vibration mode is dominated by the in-plane bending component at rest, becomes mostly a torsional mode at the release point, and it clearly displays both contributions in cruise.

B. A parametric study

Prior to the actual optimization, the 4-dimensional parametric domain that describes the CATO of the very flexible aircraft is first explored by modifying each parameter with respect to the baseline defined in table 3. Figures 13 and 14 show, respectively, the longitudinal trajectory and the wing root loads cost contribution calculated with the scaling parameters $\boldsymbol{S}_{\text{loads}} = [0.2, 0.2, 0.2]^\top$, when each parameter is independently modified from its reference value. The four parameters used in this analysis (acceleration, release speed, attitude offset and ramp angle) are divided in two groups: First, the parameters concerning the acceleration law—that is, acceleration and release speed—, and second, the parameters affecting the spatial trajectory and orientation of the aircraft during the CATO, namely, the attitude offset and ramp angle.

It can be observed how some parameters affect the scattering of the solutions in figure 13 much more than others. For example, trajectories obtained by changing the ramp angle are close to overlapping, while the solutions with changing attitude offset, θ_o, are essentially different. This might seem counterintuitive, as they both control the attitude angle during the CATO, but the difference is that θ_o has direct control over the incidence angle of the wing during the whole maneuver. The main effect of flexibility during takeoff is that the wing out-of-plane dynamics is relatively slow compared to typical launch characteristic times. In this case, depending on ramp length constraints (we consider from 5 to 20 m), the typical time scale of the CATO is between $\omega_{\text{CATO}} \in [2.5, 4.4]$ rad s^{-1}—longer ramps typically result in longer characteristic launch times—, while the first bending mode calculated with the release structural deformation as reference conditions is $\omega_{\text{OOP (I)}} = 2.75$ rad s^{-1}. In the cases shown here, the OOP bending dynamics are in general slower than the characteristic time of the CATO launch for all but the longer ramp lengths, in which case, the time scales

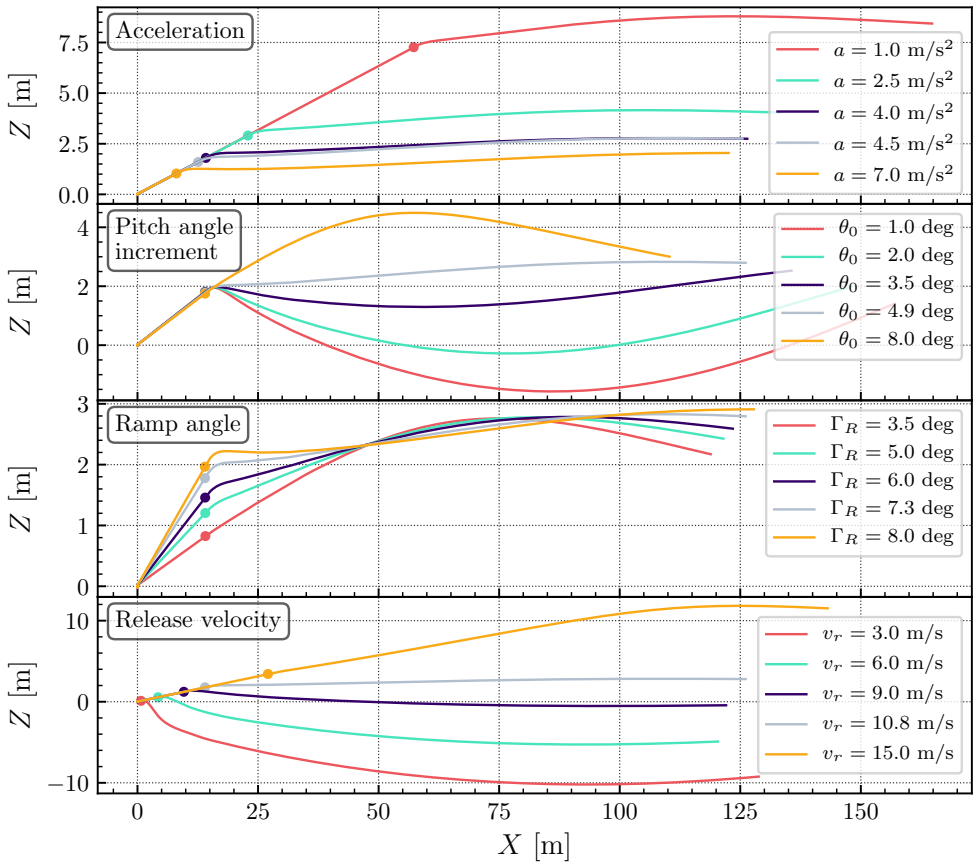

Fig. 13 Wing root trajectories of the very flexible aircraft for changes to takeoff parameters with respect to the baseline (table 3). Dots indicate start/end of launch stage.

are similar. If the aerodynamic loads on the surfaces are not applied early enough, or they are too small, the wings might not have reached a state close to the cruise flight at release time. The acceleration and release speed parametric study shows that from a ground clearance point of view, the acceleration only affects the trajectory by a vertical offset, as the longer an angled ramp is (i.e., lower acceleration for the same release speed), the higher the release point is. However, the release speed affects noticeably the trajectory, as shown in figure 13. This is due to two factors. The most direct one is that the aircraft is trimmed for cruise flight at $10\,\mathrm{m\,s^{-1}}$, and if it is released at a lower speed, it will lose altitude before reaching cruise speed, and thus, the ground clearance will be reduced. Second, higher release velocities result in higher dynamic pressure during takeoff, which deflects the wing to a close-to-cruise state faster. If at the release instant the structural deformation is not close to the cruise shape, the centre of mass of the aircraft, which is near the fuselage-wing intersection, will move downwards until the wings are generating enough lift and thus their shape is close to the steady flight one. Figure 15 shows the deformed shapes at release for release velocities.

Figure 16 shows the values of the cost function for the four-parameter study. First, a visible difference in variability of the cost can be observed. While the ramp angle Γ_R has a reduced effect in ground clearance and minimal effect in

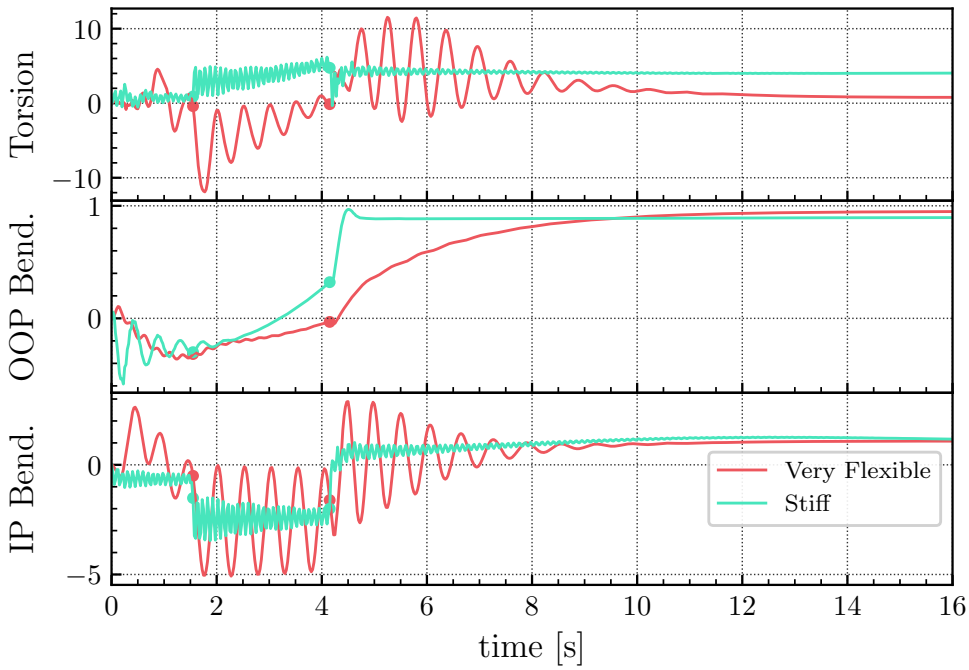

Fig. 14 Instantaneous loads cost, $J_{loads}(t)$, for changes to individual takeoff parameters from baseline. Dots indicate start/end of launch stage.

loads, the release speed affects both contributions by a larger magnitude than any of the other parameters for the range of parameters here considered. What this figure does not capture is the possibly more complex interaction of the attitude offset angle with the ramp angle with respect to the loads contribution of the cost. A direct study such as this would involve a large number of function evaluations, and this will be left to the optimization in the next section, which will capture, and exploit, this potentially complex behavior.

The interplay between acceleration and release speed is of special interest here. Figure 16 shows that greater release speed corresponds to a lower loads contribution to the cost function, but this is because, as the acceleration is kept fixed, the ramp length also increases. Once a ramp length constraint is introduced, the release speed is linked to the acceleration. This results in more abrupt accelerations for the high release speed cases, which increase the load contribution and also potentially increase the ground clearance contribution, as the slow out-of-plane wing dynamics might no have enough time to accommodate to the rapidly increasing dynamic pressure. Factoring this new coupling in the results is more complex than for the interplays between the attitude offset and ramp angles due to the acceleration effect on the loads. In addition, as the dynamic pressure increases—more or less rapidly depending on the acceleration and release speed parameters—, the influence of the attitude offset increases, as the aerodynamic loads will be greater, just as the damping introduced through added mass effects.

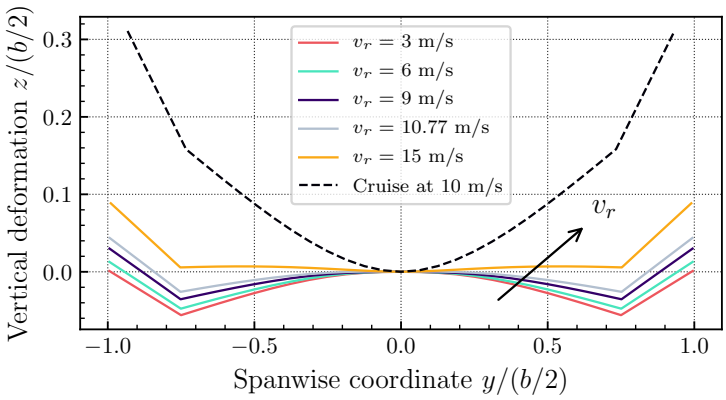

Fig. 15 Wing shape at the release instant under changes of release speed from baseline.

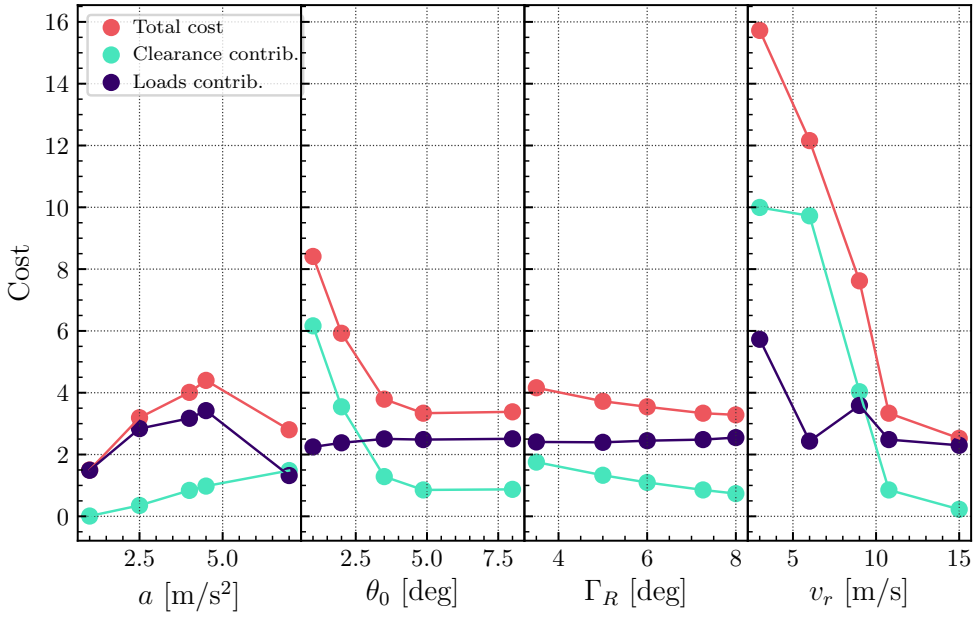

Fig. 16 Total cost and contributions for a parametric study of the CATO maneuver.

C. Optimization results

After the previous exploration, the maneuver parameter bounds have been chosen as in table 5. These values encompass a wide enough range so that the solution with a long ramp constraint is not bound by these limits. Optimal maneuvers are obtained for three fixed ramp lengths of 5, 10 and 20 m. The stall constraint in the incidence angle was active during the optimization. However, since it was not been a deciding factor in the preliminary studies, it has been left fixed at 9°.

The cost function in this work, given in equations (6) and (7), has a number of parameters that need to be selected. First, $z_{\min}$ and $z_{\max}$ have been assigned -4 and 2 m, respectively. These values ensure that the slope of the cost function is not too small in the $z < 0$ domain so that convergence is accelerated. The $z_{\max}$ parameter has been chosen so that

Variable	Domain
Acceleration, a [m s^{-2}]	[1.0, 7.0]
Release speed, v_r [m s^{-1}]	[3.0, 15.0]
Ramp angle, Γ_r [°]	[-1.0, 8.0]
Attitude offset, θ_0 [°]	[-1.0, 8.0]

Table 5 Bounds for parameters of the CATO optimization problem.

past 2 m there is not an important difference in cost function value to avoid the optimizer converging to solutions with high ground clearance but high wing root loads. Interestingly, if this saturation of the ground clearance cost is not implemented, the incidence angle constraint can be necessary to keep the simulation realistic. The ground clearance cost scaling parameter has been fixed at $S_{\text{ground}} = 10$ in order to obtain a cost of order one. Second, the wing root loads contribution $\boldsymbol{S}_{\text{loads}}$ has been assumed to be of the shape $\boldsymbol{S}_{\text{loads}} = s_{\text{loads}}[1, 1, 1]^T$ with $s_{\text{loads}} \in \mathbb{R}$ so that a single parameter needs to be tuned. A value of $s_{\text{loads}} = 0.2$ has been chosen to balance the ground clearance with the wing root loads contributions. This means that both cost contributions are comparable in magnitude and thus a single contribution will not dominate the optimization.

Figure 17 shows a scatter matrix representation of the domain sampling for the three ramp length constraints in this work. The 4-dimensional parametric domain is represented as a 4×4 array of scatter plots. Each individual plot summarizes the relation between two variables while omitting the rest. The domain sampling shown in figure 17 corresponds to the Bayesian Optimization framework being run for 30 iterations with 5 parallel function calls per iteration, that is, 150 samples per figure. Dots in the scatter plot have a variable intensity that gives an indication of the associated cost of that sample. Here, darker spots represent better solutions with lower associated cost. The diagonal plots are a representation of the sampling density in the domain of the variable in the horizontal axis. From this representation, some insight into the cost distribution and the constraints effect can be drawn. First, the ramp length constraint, expressed as a function of a and v_r can be identified in the a versus v_r plots as a defined diagonal line that divides the domain in sampled and non-sampled. The ramp length constraint has a strong effect in the overall distribution of the samples and the optimum location in the domain. It is easy to see how the shorter the maximum ramp length is, the more the optimum tends towards a corner of the domain. This is true for all the variables, however the ramp angle Γ_R behaves differently, with the darker sample dots, representing lower associated cost solutions, distributed quite horizontally across its domain. The fact that the ramp angle does not have an important effect in the CATO performance was already implied in section IV.B. The incidence angle constraint can be seen in the Γ_R versus θ_o plot of figure 17a. The visible trend concerning this constraint is that the optimum approaches it when the ramp length constraint is very restrictive. From a physical point of view, it means that the aircraft increases the wing loading through incidence angle, with a low ramp angle and a high angle of attack, such that the wing deforms and approaches the cruise deformation as quickly as possible. When the ramp length is long enough, this constraint is not necessary, as a maneuver

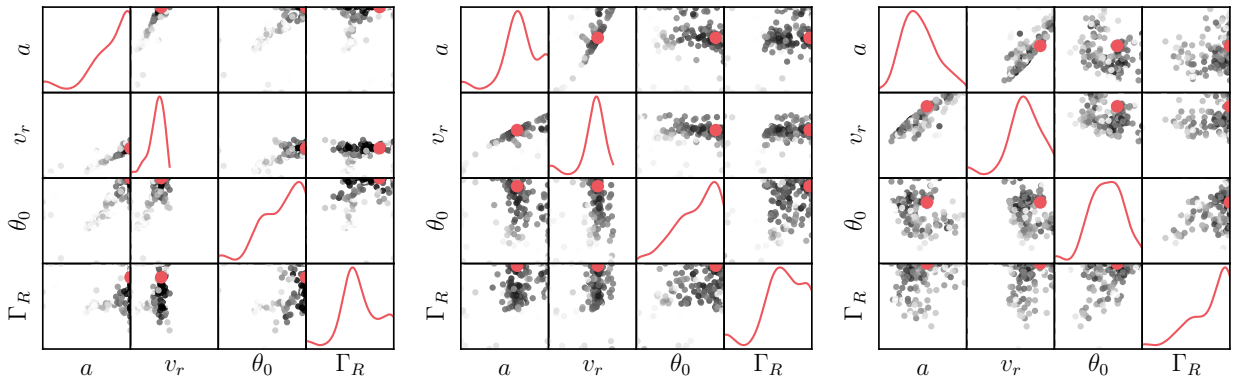

(a) Ramp length = 5 m. **(b) Ramp length = 10 m.** **(c) Ramp length = 20 m.**

Fig. 17 Scatter matrix of the BO parameter sampling for three ramp lengths. Diagonals show sampling density, darker dots show lower cost, and red dot shows optimum.

ℓ_R [m]	a [m s^{-2}]	v_r [m s^{-1}]	θ_o [°]	Γ_R [°]	Cost
5	7.00	7.20	8.00	6.55	9.19
10	4.84	9.73	7.14	7.77	2.66
20	4.28	13.07	5.43	8.00	1.72

Table 6 Results of the CATO procedure optimization for different ramp length constraints and loads-associated cost scaling.

with such high incidence angle causes very large structural loads.

Figure 18 shows the longitudinal trajectories of the aircraft wing root node in the optimal takeoff corresponding to each each ramp length, ℓ_R. Note that for $\ell = 5$ m the minimum altitude in the trajectory is negative, which would require a minimum height of the catapult to avoid having the aircraft touching the ground. Table 6 shows the CATO parameters of these optimum cases, together with their cost. First, the clearest trend is the greater ground clearance with longer ramps. As pointed previously, this is due to the longer launch times, which for a given release speed result in slower acceleration parameters. The very slow out-of-plane dynamics of the wing structure, around 0.45 Hz (see table 4) require long launch times. The constraint in ramp length, involving acceleration and release speed parameters introduces a dependency with consequences not shown in the previous parametric study, where the acceleration could be as low as possible with little change to the trajectory with respect to the release point (figure 13). The difference between those results and the ones in figure 18 is the ramp length limitation (see figure 6).

One important point worth mentioning is the influence of the shape of the ground clearance cost contribution, equation (6). Given that the function tends to zero when $z > z_{\max}$, the influence of the ground clearance in the overall result depends on the lowest altitude that the plane reaches from release until the end of the simulation. The $\ell_R = 20$ m case is released with $z > z_{\max}$, and it never dips under that value. That essentially means that the optimization for this problem is basically a loads minimization—as long as the plane never dips under $z_{\max}$, a case that would be instantly

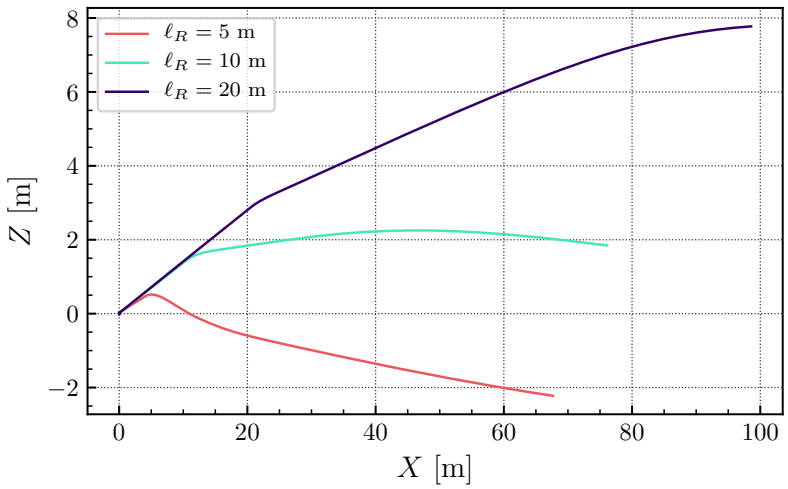

Fig. 18 Longitudinal trajectories for the optimal solutions (table 6) given different ramp length constraint values.

discarded by the optimizer—independently of the longitudinal trajectory that the aircraft follows. When the constraint is more demanding, for example, $\ell_R = 5$ m, the ground clearance is the driving criterium for the optimizer, as the associated cost grows rapidly with low z values. The medium case, $\ell_R = 10$ m is an interesting one, as the release point is close enough to $z_{\max}$ to be affected with the flattening of the cost function, while at the same time, any dip under this value will make the ground clearance contribution grow quickly. In figure 18 it can be seen how the optimum launch for this case is one that never goes too far above or below $z_{\max}$. The reason is that, if the trajectory went higher than this point, there would be no benefit in terms of ground clearance cost, while the loads would most likely increase. Likewise, if any point of the trajectory falls far below $z_{\max}$, the ground clearance cost will start to increase, decreasing the performance of the candidate.

From a loads point of view, the optimum launch procedures show a number of common features, which can be seen in the root moments shown in figure 19. First, the normalized loads in OOP bending are much lower than the torsion and IP bending ones. Given the mostly forwards acceleration suffered by the aircraft during the launch and the very low frequency of the first OOP bending mode, this is predictable. The high-frequency content in the OOP signal is linked to the second bending mode, which is excited in the initial transient. While conventional (linear) aeroelastic analysis does not focus on IP dynamics, the characteristics of this maneuver, together with the geometric coupling between torsion and IP that varies as the structure deforms during the launch, make the in-plane motion of the wing an important part of the analysis. Second, from this geometric coupling, we can see how the torsion and IP loads present similar frequency responses during the launch phase. The launch phase goes from $t = 1.75$ s to $t = 2.6$, 3.9 and 4.7 seconds respectively for increasing ramp length, which can be easily seen on the time trace of all three root moments. Aerodynamic damping however is very low on the in-plane bending dynamics of the wing and has a much more dominant effect on the torsional

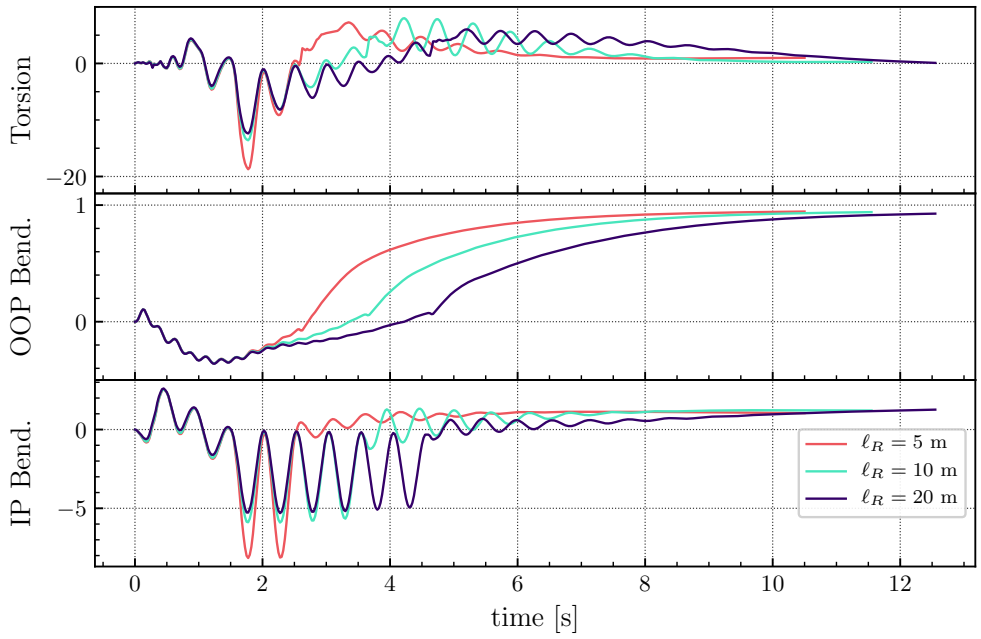

Fig. 19 Wing root loads for the optimum cases (table 6) given different ramp lengths. Loads normalized with cruise wing root loads.

response. This is due to the lack of first order aerodynamic effects acting on IP deformations, as they only generate an increase in incidence velocity. The torsion loads instead are aerodynamically damped due to the effect on the rotational velocity of the wing cross-sections, and their influence in the incidence angle of the wing has a coupling effect with the very damped OOP dynamics. It is also important to note how quickly the loads converge to the cruise values. This is due to the effect the long fuselage has on the damping of the longitudinal rigid body dynamics of the aircraft.

Amongst the differences between different ramp length cases, it is worth mentioning the different values of IP bending peaks during the launch phase. While the difference between the 10 and 20 m cases is not too large, the 5 m case has a peak IP bending loads value of up to 8 times the cruise IP bending loads. Despite this, up to release, the IP oscillations are of the same frequency, which is the 2$^{\text{nd}}$ structural mode indicated in table 4 and depicted in figure 12. However, past the release point, the motion becomes more damped and the frequency increases, which is consistent with the change of frequency that the second structural mode suffers when the wings of the aircraft start deforming due to the aerodynamic loading. Concerning the torsional dynamics, it is interesting to note how the peak value for all the procedures, but specially for the shorter one, is more than 10 times the cruise loads. The release instant can be identified in the torsion loads due to the higher frequency of the response, it shows an abrupt change of slope followed by a high-frequency oscillation. This is the kind of high-frequency-driven dynamics that needs a finer time discretization in the structural solver.

V. Conclusion

A nonlinear aeroelastic simulation strategy has been presented that allows to simulate and optimize complex maneuvers of very flexible aircraft. The most relevant modelling choices and numerical parameters have been identified and discussed for each main component of the aeroelastic solver (structural and aerodynamic models and coupling algorithm), as well as their effect on the simulation of highly flexible aeroelastic aircraft. Bayesian optimization has been shown to provide a suitable strategy to define dynamic maneuvers that can be parameterized with relatively small number of design variables. The resulting maneuver, which is defined under ideal conditions (e.g., calm air) can then be used as the tracked reference for a closed-loop control scheme.

Catapult-assisted takeoff has been used as a representative example of a highly dynamical nonlinear aeroelastic problem. In this problem, the aircraft is attached to the catapult on multiple nodes and the velocity of these nodes is prescribed so that a trajectory and acceleration law is enforced. Once the release speed is reached, the aircraft is released and left to fly in open loop. This problem features a high range of flight speeds (from zero to close to cruise speed), high range of structural deformations (from gravity-only loading to aeroelastic equilibrium in cruise) and changing driving mechanisms as the simulation progresses. Due to this, linear aeroelastic simulation methods would not be able to capture the complex phenomena that arise from the interaction of structure, aerodynamics, prescribed rigid-body motion and flight dynamics.

The proposed CATO procedure is described using 4 parameters, namely, the acceleration value, the release speed, the ramp angle and the offset attitude of the aircraft. The ramp is also assumed to be straight, the pitch angle of the aircraft constant and the acceleration rate constant until release. In order to define an optimum launch procedure, a cost function that accounts for ground clearance and wing root loads has been defined. Constraints on ramp length and effective incidence angle are also imposed to avoid physically unfeasible solutions.

A parametric investigation has shown that ground clearance is very sensitive to release speed and pitch angle. Wing root loads are increased by large acceleration values while a high release speed reduces them. Longer ramps are therefore preferred, and a ramp length constraint has been included in the optimization. Depending on the acceleration and release speed combination, the characteristic time of the CATO is from 60 to 108% of the period of the first bending mode of the wing. This, together with the large damping of out-of-plane motions, explains why larger ramps with higher release speed perform well also from a ground clearance point of view. In limited length ramps, the CATO is too fast for the wing to adopt the quasi-steady deflection for those instantaneous conditions. On release, the centre of mass, which is located close to the wing root due to the payload, plunges due to the insufficient lift generated by the wings, which then deform and achieve a deflection close to the corresponding steady one. This plunging and recovering motion can excite rigid body modes such as the phugoid, and depending on the controllability of the aircraft and the ground clearance it might be a limiting factor to consider when designing the CATO procedure.

The optimization studies have shown that, for a given model and constraints, there is a minimal ramp length under

which the aircraft would hit the ground and that the parameter that has the strongest effect in the solution is the release speed. Unsurprisingly, with greater release velocities the ground clearance is larger and the wing root loads are smaller, as long as the ramp length constraints allow the acceleration to be small enough. More interestingly however, the ramp angle parameter has a very small effect on the launch, unlike the pitch angle parameter. A large pitch angle parameter encourages wing loading during the early stages of the CATO, which results in a closer to quasi-steady structural state at release. However, a large incidence angle also increases the wing root loads. In our results the incidence angle is not affected by the optimization constraints, as the increase of loads balances the ground clearance effect.

This paper has shown a procedure to determine nominal trajectories that can be input to a flight control system for operation on realistic conditions. This would need to include the actual wind conditions in the atmospheric boundary layer, which we have recently investigated in Ref. [13]. Future work will assess the requirements on the flight control system for safe takeoff under acceptable levels of atmospheric turbulence.

Acknowledgement

This work has been funded by Airbus Defence and Space and by the UK Engineering and Physical Sciences Research Council (grant number EP/R007470/1).

References

[1] Patil, M. J., Hodges, D. H., and Cesnik, C. E. S., "Nonlinear Aeroelasticity and Flight Dynamics of High-Altitude Long-Endurance Aircraft," *Journal of Aircraft*, Vol. 38, No. 1, 2001. doi:10.2514/2.2738.

[2] Wang, Z., Chen, P. C., Liu, D. D., and Mook, D. T., "Nonlinear-Aerodynamics/Nonlinear-Structure Interaction Methodology for a High-Altitude Long-Endurance Wing," *Journal of Aircraft*, Vol. 47, No. 2, 2010. doi:10.2514/1.45694.

[3] Zhao, Z., and Ren, G., "Multibody Dynamic Approach of Flight Dynamics and Nonlinear Aeroelasticity of Flexible Aircraft," *AIAA Journal*, Vol. 49, No. 1, 2011, pp. 41–54. doi:10.2514/1.45334.

[4] Su, W., and Cesnik, C. E. S., "Dynamic Response of Highly Flexible Flying Wings," *AIAA Journal*, Vol. 49, No. 2, 2011, pp. 324–339. doi:10.2514/1.j050496.

[5] Hesse, H., Palacios, R., and Murua, J., "Consistent Structural Linearization in Flexible Aircraft Dynamics with Large Rigid-Body Motion," *AIAA Journal*, Vol. 52, No. 3, 2014. doi:10.2514/1.J052316.

[6] Changchuan, X., Lan, Y., Yi, L., and Chao, Y., "Stability of Very Flexible Aircraft with Coupled Nonlinear Aeroelasticity and Flight Dynamics," *Journal of Aircraft*, Vol. 55, No. 2, 2018, pp. 862–874. doi:10.2514/1.C034162.

[7] Hoover, C. B., and Shen, J., "Parametric Study of Propeller Whirl Flutter Stability with Full-Span Model of X-57 Maxwell Aircraft," *Journal of Aircraft*, Vol. 55, No. 6, 2018, pp. 2530–2537. doi:10.2514/1.C035081.

[8] Cesnik, C. E. S., Palacios, R., and Reichenbach, E. Y., "Reexamined Structural Design Procedures for Very Flexible Aircraft," *Journal of Aircraft*, Vol. 51, No. 5, 2014. doi:10.2514/1.c032464.

[9] Afonso, F., Vale, J., Oliveira, E., Lau, F., and Suleman, A., "A review on non-linear aeroelasticity of high aspect-ratio wings," *Progress in Aerospace Sciences*, Vol. 89, 2017. doi:10.1016/j.paerosci.2016.12.004.

[10] Riso, C., Di Vincenzo, F. G., Ritter, M., Cesnik, C. E. S., and Mastroddi, F., "Nonlinear Aeroelastic Trim of Very Flexible Aircraft Described by Detailed Models," *Journal of Aircraft*, Vol. 55, No. 6, 2018, pp. 2338–2346. doi:10.2514/1.C034787.

[11] Su, W., and Cesnik, C. E. S., "Nonlinear Aeroelasticity of a Very Flexible Blended-Wing-Body Aircraft," *Journal of Aircraft*, Vol. 47, No. 5, 2010. doi:10.2514/1.47317.

[12] Hesse, H., and Palacios, R., "Dynamic Load Alleviation in Wake Vortex Encounters," *Journal of Guidance, Control, and Dynamics*, Vol. 39, No. 4, 2016. doi:10.2514/1.g000715.

[13] Deskos, G., del Carre, A., and Palacios, R., "Assessment of Low-Altitude Atmospheric Turbulence Models for Aircraft Aeroelasticity," *Journal of Fluids and Structures*, Vol. 95, 2020. doi:10.1016/j.jfluidstructs.2020.102981.

[14] Haghighat, S., Martins, J. R. R. A., and Liu, H. H. T., "Aeroservoelastic Design Optimization of a Flexible Wing," *Journal of Aircraft*, Vol. 49, No. 2, 2012, pp. 432–443. doi:10.2514/1.C031344.

[15] Cook, R. G., Palacios, R., and Goulart, P., "Robust Gust Alleviation and Stabilization of Very Flexible Aircraft," *AIAA Journal*, Vol. 51, No. 2, 2013. doi:10.2514/1.j051697.

[16] Silvestre, F. J., Guimaraes Neto A. B, Mendes Bertolin, R., da Silva, R. G., and Paglione, P., "Aircraft Control Based on Flexible Aircraft Dynamics," *Journal of Aircraft*, Vol. 54, No. 1, 2017. doi:10.2514/1.C033834.

[17] Barbosa, G. C., Bertolin, R., González, P. J., Guimaraes Neto, A. B., and Silvestre, F. J., "Fuzzy Gain-Scheduling Applied for a Very Flexible Aircraft," *2018 AIAA Guidance, Navigation, and Control Conference*, 2018.

[18] Wang, Y., Wynn, A., and Palacios, R., "Nonlinear Aeroelastic Control of Very Flexible Aircraft Using Model Updating," *Journal of Aircraft*, Vol. 55, No. 4, 2018. doi:10.2514/1.C034684.

[19] Yagil, L., Raveh, D. E., and Idan, M., "Deformation Control of Highly Flexible Aircraft in Trimmed Flight and Gust Encounter," *Journal of Aircraft*, Vol. 55, No. 2, 2018, pp. 829–840. doi:10.2514/1.C034353.

[20] Maraniello, S., and Palacios, R., "Optimal Rolling Maneuvers with Very Flexible Wings," *AIAA Journal*, Vol. 55, No. 9, 2017. doi:10.2514/1.j055721.

[21] Powell, M. J., "An efficient method for finding the minimum of a function of several variables without calculating derivatives," *The Computer Journal*, Vol. 7, No. 2, 1964.

[22] Nelder, J. A., and Mead, R., "A simplex method for function minimization," *The computer journal*, Vol. 7, No. 4, 1965.

[23] Snoek, J., Larochelle, H., and Adams, R. P., "Practical Bayesian Optimization of Machine Learning Algorithms," *Advances in Neural Information Processing Systems*, 2012.

[24] Frazier, P. I., "A tutorial on bayesian optimization," *arXiv preprint arXiv:1807.02811*, 2018.

[25] Géradin, M., and Cardona, A., *Flexible multibody dynamics: A finite element approach*, John Wiley, 2001.

[26] Simeon, B., "On Lagrange Multipliers in Flexible Multibody Dynamics," *Computer Methods in Applied Mechanics and Engineering*, Vol. 195, No. 50-51, 2006.

[27] Katz, J., and Plotkin, A., *Low-Speed Aerodynamics*, Cambridge Aerospace Series, Cambridge University Press, 2001.

[28] Simpson, R. J. S., Palacios, R., and Murua, J., "Induced Drag Calculations in the Unsteady Vortex Lattice Method," *AIAA Journal*, Vol. 51, No. 7, 2013. doi:10.2514/1.J052136.

[29] Wiener, N., *Extrapolation, interpolation, and smoothing of stationary time series with engineering applications*, Technology Press of the Massachusetts Institute of Technology, Cambridge, Mass, 1964.

[30] del Carre, A., Muñoz, A., Goizueta, N., and Palacios, R., "SHARPy: A Dynamic Aeroelastic Simulation Toolbox for Very Flexible Aircraft and Wind Turbines," *Journal of Open Source Software*, Vol. 4, No. 44, 2019. doi:10.21105/joss.01885.

[31] Cesnik, C. E. S., Senatore, P. J., Su, W., Atkins, E. M., and Shearer, C. M., "X-HALE: A Very Flexible Unmanned Aerial Vehicle for Nonlinear Aeroelastic Tests," *AIAA Journal*, Vol. 50, No. 12, 2012. doi:10.2514/1.j051392.

[32] Del Carre, A., Teixeira, P. C., Palacios, R., and Cesnik, C. E. S., "Nonlinear Response of a Very Flexible Aircraft Under Lateral Gust," *International Forum on Aeroelasticity and Structural Dynamics*, Savannah, Georgia, USA, 2019. IFASD Paper 2019-090.

[33] Wales, D. J., and Doye, J. P. K., "Global Optimization by Basin-Hopping and the Lowest Energy Structures of Lennard-Jones Clusters Containing up to 110 Atoms," *The Journal of Physical Chemistry A*, Vol. 101, No. 28, 1997. doi:10.1021/jp970984n.

[34] Jones, E., Oliphant, T., Peterson, P., et al., "SciPy: Open source scientific tools for Python," , 2001–. URL `http://www.scipy.org/`.

[35] The GPyOpt authors, "GPyOpt: A Bayesian Optimization framework in Python," `http://github.com/SheffieldML/GPyOpt`, 2016.